Water Research 219 (2022) 118558

Contents lists available at ScienceDirect

Water Research

journal homepage: www.elsevier.com/locate/watres

Photocatalytic degradation of persistent organic pollutants by Co-Cl bond reinforced CoAl-LDH/$Bi_{12}O_{17}Cl_2$ photocatalyst: mechanism and application prospect evaluation

Jiayin Guo[a,b,c], Haibo Sun[d], Xingzhong Yuan[a,c], Longbo Jiang[a,c], Zhibin Wu[d], Hanbo Yu[e], Ning Tang[a,c], Mengdie Yu[a,c], Ming Yan[a,c], Jie Liang[a,c,*]

[a] *College of Environmental Science and Engineering, Hunan University, Changsha 410082, P.R. China*
[b] *School of Resources and Environment, Hunan University of Technology and Business, Changsha, 410205, P.R. China*
[c] *Key Laboratory of Environmental Biology and Pollution Control (Hunan University), Ministry of Education, Changsha 410082, P.R. China*
[d] *College of Resources and Environment, Hunan Agricultural University, Changsha, 410128, P.R. China*
[e] *School of Hydraulic and Environmental Engineering, Changsha University of Science & Technology, Changsha 410114, China*

ARTICLE INFO

Key words:
Photocatalysis
$Bi_{12}O_{17}Cl_2$
CoAl-LDH
Ciprofloxacin degradation
Actual sunlight
Toxicity assessment

ABSTRACT

The widespread distribution of persistent organic pollutants (POPs) in natural waters has aroused global concern due to their potential threat to the aquatic environment. Photocatalysis represents a promising mean to remediate polluted waters with the simple assistance of solar energy. Herein, we fabricated a Co-Cl bond reinforced CoAl-LDH/$Bi_{12}O_{17}Cl_2$ heterogeneous photocatalyst to investigate the feasibility of photocatalysis to treat POPs-polluted water under environmental conditions. The optimum CoAl-LDH/$Bi_{12}O_{17}Cl_2$ (5-LB) composite photocatalyst exhibited excellent photocatalytic performance, which could degrade 92.47 % of ciprofloxacin (CIP) and 95 % of bisphenol A (BPA) with 2h of actual solar light irradiation in Changsha, China (N 28.12 °, E 112.59 °). In view of the synergistic influence of water constituents, various water matrices greatly affected the degradation rate of CIP (BPA), with the degradation efficiency of 82.17% (84.37%) in tap water, 69.67% (71.63%) in wastewater effluent, and 44.07% (67.7%) in wastewater inflow. The results of electron spin resonance, and chemical trapping experiment, HPLC-MS and density functional theory calculation reflected that the degradation of CIP was mainly attributed to h^+ and $^1O_2$ attacking the active atoms of CIP molecule with high Fukui index. Furthermore, the non-toxicity of both 5-LB photocatalyst and treated CIP solution was proved by *E.coli* and *B. subtilis* cultivation, which further demonstrated the feasibility of the 5-LB to treat POPs in real water under irradiation of solar light.

1. Introduction

Persistent organic pollutants (POPs, e.g., pharmaceuticals and endocrine disrupters) with high toxicity, carcinogenicity and bioaccumulation in the aquatic ecosystem are both tedious and expensive to treat (Dong et al., 2015a). Towards the treatment of POPs in water and wastewater, many advanced technologies with high efficiency and low-cost have been developed to date, including adsorption, microbial degradation, electrolysis and photocatalysis (Dong et al., 2015a, Pi et al., 2018). Among these methods, environmentally friendly photocatalysis is superior in terms of its outstanding ability on complete “destroying” the contaminates with the simple aid of solar energy (Sun et al., 2020, Yang et al., 2022).

In practical application, ideal photocatalysts are required to achieve excellent solar light absorption and fast conversion (Dong et al., 2015b, Wu et al., 2018). Two-dimensional (2D) layered materials demonstrate unique ability of confinement of electrons in their layer, leading to exceptional optical and electronic properties (Xiong et al., 2018). Besides, the strong in-plane covalent bonding furnishes sites for the construction of heterostructures, the resulting 2D/2D heterojunction with greater contact area possesses plentiful tight and high-speed charge transfer channels at interfacial junction for convenient migration of charge (Ganguly et al., 2019). Bismuth oxyhalide is one of a new class of 2D layered materials for photocatalytic energy conversion and

---

* Corresponding author. Tel.: +86 731 88821413; Fax: +86 731 88821413.
E-mail address: liangjie82@163.com (J. Liang).

https://doi.org/10.1016/j.watres.2022.118558
Received 2 November 2021; Received in revised form 23 April 2022; Accepted 4 May 2022

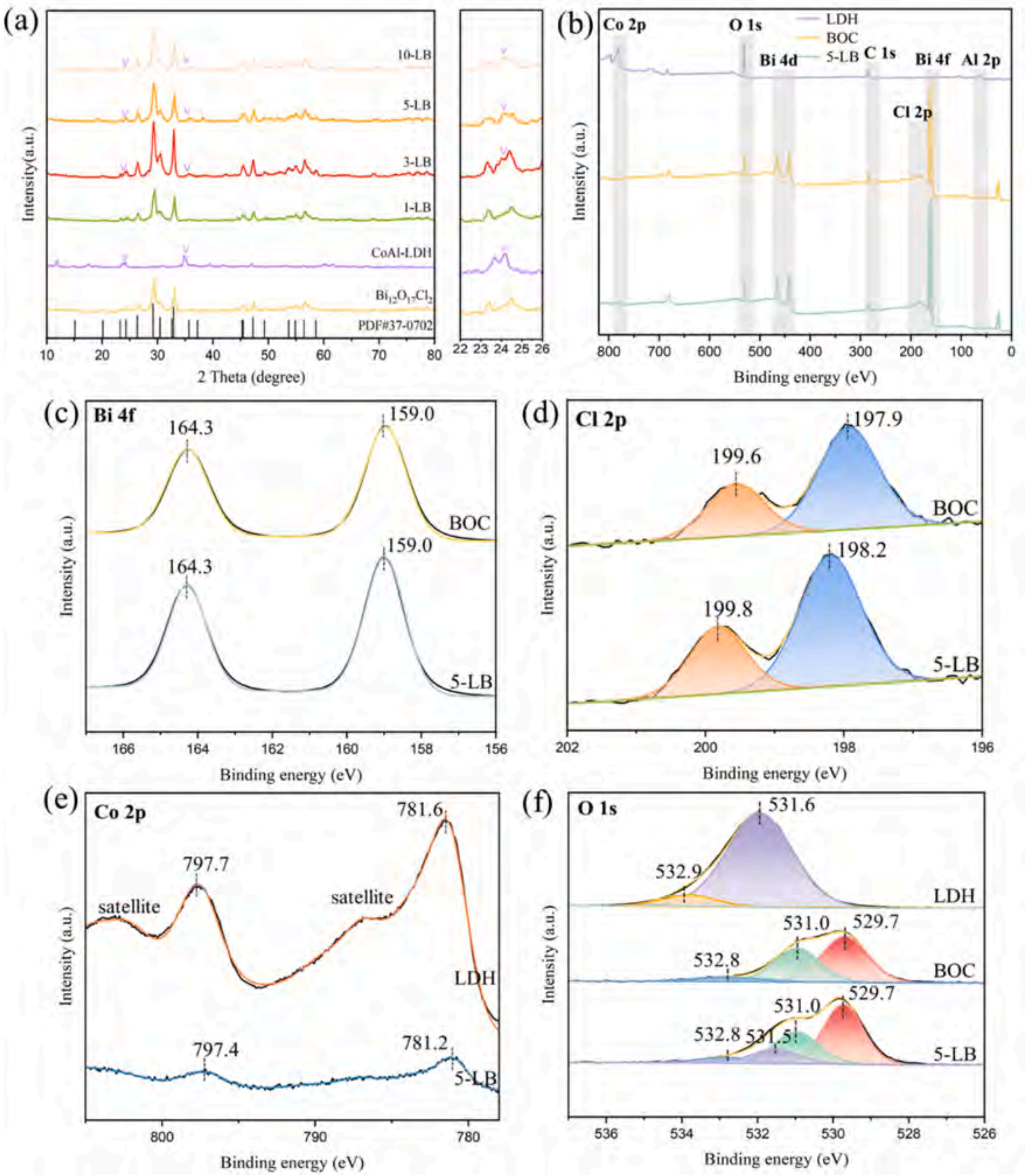

Fig. 1. (a) XRD patterns of the prepared photocatalysts. (b) XPS survey spectra of pure $Bi_{12}O_{17}Cl_2$, CoAl-LDH and 5-LB composite; high-resolution XPS spectra: (c) Bi 4f (d) Cl 2p (e) Co 2p (f) O1s.

environment remediation. Specially, the bismuth-rich ones, such as $Bi_{12}O_{17}Cl_2$ (Guo et al., 2021) and $Bi_{24}O_{31}Br_{10}$ (Shang et al., 2014), have been confirmed to possess higher photon absorption efficiency and more negative conduction band positions that can meet most of the reaction potential. It is worth noting that the yellow $Bi_{12}O_{17}Cl_2$ illustrate outstanding visible light photocatalytic performance for pollutant degradation. Whereas, the fast recombination of photogenerated charges still hindered the further application of $Bi_{12}O_{17}Cl_2$. Li et al., reported that the internal electric field between $(Bi_{12}O_{17})$ and (Cl_2) can actuate the transfer of electrons from $Bi_{12}O_{17}Cl_2$ to other semiconductors (Li et al., 2016). Furthermore, the interlaminar Cl^- can form chemical bonding with foreign cations which further favors the heterogenous migration of carriers (Zhu et al., 2021). Therefore, we hypothesized that the construction of a heterostructure between $Bi_{12}O_{17}Cl_2$ and another 2D semiconductor with a matching band structure will be a promising way to enhance the separation efficiency of photoexcited carriers meanwhile acquire improved photocatalytic performance of $Bi_{12}O_{17}Cl_2$.

Layered double hydroxides (LDHs, $[M_{1-x}{}^{2+}M_x{}^{3+}(OH)_2](A^{n-})^{x/n}\cdot mH_2O]$), also known as hydrotalcite-like clays, are another kind of 2D laminated materials, which possess the merits of low cost, facile preparation, large surface area, flexible interlayer structure for electron transfer, visible-light response performance and abundant active sites (Tang et al., 2016). In recent years, LDHs are highlighted for their capacity to enhance catalytic activity in cooperation with other functional materials. Lee et al., reported that the CoAl-LDHs with the band gap of 2.1 eV can serve as the visible light absorber to hybridize with P25 (Kumar et al., 2017). Wu et al., clarified that the unoccupied *d* orbitals of Co or Al atoms of CoAl-LDH can couple with the N atoms of $g\text{-}C_3N_4$ to form covalent bonding states, thereby promoting the separation and transfer of photoexcited charges (Wu et al., 2018). Thus, it is expected to improve the photochemical properties of $Bi_{12}O_{17}Cl_2$ by coupling with CoAl-LDH.

In this study, we firstly fabricated the eco-friendly CoAl-LDH/$Bi_{12}O_{17}Cl_2$ (x-LB) photocatalysts via a facile hydrothermal method, and the performance of LB hybrids for POPs removal was evaluated by their degradation ability for ciprofloxacin (CIP) and bisphenol A (BPA) under simulate visible light. Meanwhile, the radical trapping experiments, ESR measure, HPLC-MS and density functional theory (DFT) calculation were conducted to deduce the photocatalytic pathway and mechanism. Then, the influence of the water characteristics (e.g., pH, anions, natural dissolved organic matter and microplastics) on photocatalytic performance was investigated to evaluate the potential application of x-LB in a real environment. On this basis, degradation of POPs in different natural water matrices under the irradiation of natural solar light was also carried out to verify the practical feasibility. Last but not least, the toxicity of the treated POPs solution and the leaching solution of x-LB was assessed by toxic effects on typical bacteria. The potential for eliminating the threat of POPs in natural environmental conditions without causing secondary pollution via bismuth oxyhalides-based photocatalyst was verified in this study.

2. Experimental section

2.1. Synthesis of CoAl-LDH/$Bi_{12}O_{17}Cl_2$

All used chemicals were listed in Text S1, and were used as received. The CoAl-LDH/$Bi_{12}O_{17}Cl_2$ hybrids were synthesized by an *in-situ* method, and the detailed process was described in Text S2.

2.2. Photocatalytic activity measurement

To investigate the photocatalytic activity of CoAl-LDH/$Bi_{12}O_{17}Cl_2$ hybrids, a series of photodegradation experiments were conducted by using CIP and BPA as target pollutants under the visible-light irradiation, and the detailed process was presented Text S3.

Reactive oxygen species (ROS) were studied by electron spin (ESR) spectroscopy (JES-FA200, JEOL; Japan). Apparent, time-based CIP rate constants were determined with and without quenching agents to reflect reaction mechanisms. Detailed information about ROS investigation was presented in Text S4. The obtained data were used to determine the contribution of reactive species (h^+, $\bullet OH$, $\bullet O_2^-$ and $^1O_2$) to the degradation of CIP according to the eqs. 1-4

$$R_{\bullet OH} = \frac{k_{\bullet OH}}{k_{app}} \approx \frac{\left(k_{app} - k_{IPA}\right)}{k_{app}} \quad (1)$$

$$R_{^1O_2} = \frac{k_{^1O_2}}{k_{app}} \approx \frac{\left(k_{IPA} - k_{NaN_3}\right)}{k_{app}} \quad (2)$$

$$R_{\bullet O_2^-} = \frac{k_{\bullet O_2^-}}{k_{app}} \approx \frac{\left(k_{app} - k_{TEMPOL}\right)}{k_{app}} \quad (3)$$

$$R_{h^+} = \frac{k_{h^+}}{k_{app}} \approx \frac{\left(k_{app} - k_{Na_2C_2O_4}\right)}{k_{app}} \quad (4)$$

In eqs.1-4, R represents the fractional contribution of a particular reactive species to the apparent rate constant (k_{app}) and ki is the rate constant of the degradation of CIP by a certain reactive species or in the existence of a trapping reagent.

To identify the effects of environmental factors, Cl^- (NaCl, 10 mM), NO_3^-($NaNO_3$, 10 mM), SO_4^{2-} (Na_2SO_4, 10mM), CO_3^{2-} (Na_2CO_3, 10mM), HA (humic acid, 5, 10 or 15 mg L^{-1}) or microplastic particles (polystyrene, PS, 10 or 20 mg L^{-1}) was added to the CIP (15 mg L^{-1}) solution containing 400 mg L^{-1} 5-LB. When investigating the effects of real water matrices and natural sunlight on the photocatalytic performance of 5-LB, experimental solutions were obtained by adding CIP or BPA powder to 0.45 μm membrane-filtered tap water (Changsha, China), wastewater inflow (Changsha, China) and wastewater effluent (Changsha, China), and the photocatalysis experiments were carried out from 13:00 p.m. to 15:00 p.m. on sunny days in September (2021) in Changsha, China (N 28.12 °, E 112.59 °). Light intensity was 30-35 mW cm^{-2} measured by the PL-MW 2000 light power meter from Beijing Perfectlight Technology Co.,Ltd. (China).

2.3. Biotoxicity assessment

Typical Gram-negative bacteria Escherichia coli (*E.coli*) and Gram-positive bacteria Bacillus subtilis (*B.subtilis*) were selected as biological subsequent models to evaluated the toxicity, and the detailed information was presented in Text S5.

2.4. Theoretical calculation method

The Fukui index of CIP was calculated by Gaussian 16W program, and the calculation details were described in Supporting Information (Text S6) (Lu and Chen, 2011).

3. Results and discussion

3.1. Crystalline, chemical and morphology structures

The crystalline structures of the as-prepared samples were analyzed by XRD (Fig. 1a). The BOC patterns exhibited a series of strong diffraction peaks at 2θ values of 23.2°, 24.3°, 26.4°, 29.2°, 30.4°, 32.9°, 45.5°, 47.2°, 54.9°, 56.5°, corresponding respectively to the (111), (113), (115), (117), (0012), (200), (2012), (220), (315) and (317) lattice planes of the standard tetragonal $Bi_{12}O_{17}Cl_2$ (JCPDS 37-0702). For the pure LDH, the peaks at 11.7°, 23.5° and 34.6° can be assigned to (003), (006) and (009) lattice planes of a stacked LDH phase with CO_3^{2-} in the interlayer region (Dou et al., 2015). X-LB hybrids demonstrated a similar XRD patterns of BOC, indicating the integration of these two semiconductors with high purity and degree of crystallinity. The peaks of LDH were inconspicuous due to its low contents, and only when the content of LDH reached 3 wt%, the peaks at 23.5° and 34.6° of LDH can be observed. Collectively, the two semiconductors were well combined, and the introduction of LDH did not affect the phase of BOC.

For further determine the surface elemental compositions and valence states of the as-prepared photocatalysts, and provide a better understanding of the interaction between BOC and LDH, X-ray photoelectron spectroscopy (XPS) analysis was introduced. Based on the XPS survey spectra (Fig. 1b), the presence of Co element in 5-LB further confirmed the successful fabrication of the composite. Furthermore, the high-resolution XPS spectra of Bi 4f, Cl 2p, Co 2p and O 1s, were revealed in Fig. 1c-f. As shown in the high resolution spectra of Bi 4f, the binding energy for Bi 4f 5/2 and 4f 7/2 of BOC were 164.3 and 159.0 eV. The peak positions did not alter after the introduction of LDH, indicating that LDH exhibited negligible effect on the original structure of ($Bi_{12}O_{17}$) slab. Whereas, the characteristic peak at 199.6 and 197.9 eV corresponding to Cl 2p1/2 and Cl 2p3/2 of Cl^- ions upshifted to a higher energy level (199.8 and 198.2 eV) after the modification of LDH. The shifts of binding energy verified that coupling interaction occurred between BOC and LDH, which affected the electronic energy distribution of BOC. Simultaneously, the position of Co $2p_{3/2}$ and Co $2p_{1/2}$ characteristic peaks in 5-LB composites downshifted from 781.6 and 797.7 eV to 781.2 and 797.4 eV, respectively (Wang et al., 2017), which indicated that the electrons of Cl atoms as electron donor can interact with the unoccupied *d* orbitals of Co atoms to form Co-Cl bond with the minimal space constraints (Liu et al., 2019, Wu et al., 2018). This was further confirmed by the high-resolution XPS spectra of O 1s (Fig. 1f). The O 1s peak of LDH at 531.6 and 532.9 eV corresponded respectively to the Co-O and Al-O species in LDH, and the peaks of BOC at 529.7, 531.0 and

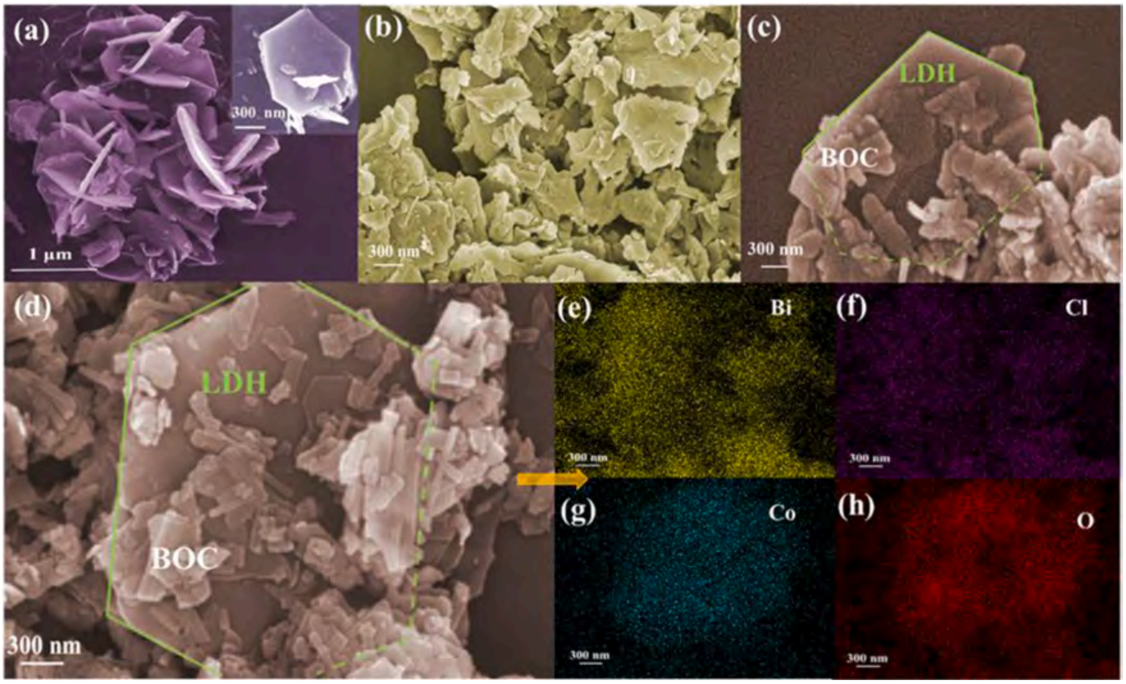

Fig. 2. The SEM images of (a) LDH, (b) BOC and (c and d) 5-LB. (e-h) Corresponding elemental maps of 5-LB.

532.8 eV were ascribed to lattice Bi-O-Bi bond, surface hydroxyl and adsorbed H_2O, respectively (Guo et al., 2021, Wang et al., 2017). Interestingly, the binding energies of lattice Co-O species for 5-LB were 531.5 eV, and the conversion trend of the binding energy value of Co-O is in keeping with that of Co 2p. However, the peaks for Bi-O-Bi bond, surface hydroxyl and adsorbed H_2O on 5-LB maintained unchanged, demonstrating that LDH did not connect to BOC via O containing chemical bonds. Thus, all the results above clarified that the formation of intimate heterostructure between LDH and BOC was attribute to the formation of Co-Cl bond at the interface, and Co atoms on the heterojunction possess lower binding energy compared to pristine LDH may be ascribed to the acquisition of electrons in the heterogeneous system, resulting the increase of electron density (Wang et al., 2020). Reversely, the electrons escape of Cl atoms leads to the decrease of electron density, reflecting as higher binding energy.

The SEM images of pure LDH, BOC and 5-LB were exhibited in Fig. 2. Clearly, the fabricated LDH crystal nanosheets were of hexagonal shapes. The pure BOC exhibited irregular and compactly agglomerated two-dimensional structure. After dispersing the LDH nanosheets into aqueous solution via ultrasonication. Under the solvothermal condition, LDH sheets acted as a substrate to induce the in-situ growth of BOC in a plane-to-plane manner, as shown in Fig. 2c and d. A large amount of BOC sheets dispersed on the surface of LDH substrate, which facilitated the dispersal of BOC. Furthermore, EDX element mapping was carried out on the area shown by Fig. 2d, which demonstrated that Bi, Cl, Co, O were distributed throughout the 5-LB samples (Fig. 2e-h). Additionally, the bright hexagonal region of Co element further indicated that the hexagonal nanosheet in Fig. 2d could be ascribed to LDH. The TEM images further confirmed the microstructure of the hexagonal LDH sheets (Fig. S1a) and the 2D structure of the pure BOC (Fig. S1b). As for 5-LB hybrids (Fig. S1c), both hexagonal LDH sheets and 2D BOC could be observed. Meanwhile, two types of contrast fringes in the HRTEM image of 5-LB hybrids (Fig. S1d) was found. The lattice spacing of 0.259 nm was correspond to the (012) plane of the LDH phase, and the lattice fringes of 0.338 nm were ascribed to the (115) plane of the BOC phase.

The surface area and porosity of the photocatalysts play a significant role in their photocatalytic performance. As displayed in the N_2 adsorption-desorption isotherms (Fig. S2a), the typical IV isotherm with an H3 hysteresis loop existed in all samples, which confirmed the presence of mesoporous structure. The specific surface area, pore volume and average pore size were shown in Table S1 and Fig. S2b. Obviously, BOC possessed a small specific surface area (4.391 m^2g^{-1}) and poor mesoporous feature, which may limit the photocatalytic activity, while LDH possessed the relatively larger specific surface area (38.975 m^2g^{-1}). Fortunately, the addition of 5 wt% LDH increased the specific surface area of BOC to 2.2 times (9.666 m^2g^{-1}), and the mesoporous features became more obvious, which may promote the exposure of the active sites and the diffusion of contaminants and active radicals during the photocatalytic process.

3.2. Photocatalytic performance

Herein, CIP molecules have been adopted to assess the capability for eliminating POPs of the as-prepared x-LB composites with different content of LDH. Fig. 3a depicted the changes of the CIP concentration over time (dark and irradiation time) in the presence of the as-synthesized photocatalysts. After 120 min dark reaction and 120 min visible light irradiation ($\lambda > 420$ nm), approximately 7.19% and 62.76% of CIP was removed over bare LDH and bare BOC, respectively. Besides, it was obvious that coupling LDH with BOC could effectively improve the removal efficiency of CIP, and the optimal removal effect appeared in 5-LB, where 96.37% of CIP was removed from the solution.

It was worth noting that x-LB composites had stronger adsorption capacity than pure BOC. In order to eliminate the influence of adsorption on the experimental data in the light stage, we firstly conducted the adsorption tests of above photocatalysts for CIP under the dark condition. As illustrated in Fig. 3b, LDH, BOC and 5-LB reached adsorption equilibrium at about 120 min, implying that the adsorption process wouldn't further interfere with the subsequent analysis of photocatalytic results. Furthermore, the adsorption kinetics results were fitted with pseudo-first-order model (solid lines in Fig. 3b) and pseudo-second-order model (dashed lines in Fig. 3b), respectively, and the fitted parameters were listed in Table S2. Pseudo-second-order kinetics process was more suitable for the adsorption process of LDH (R^2=0.99252) and BOC (R^2=0.9994), which reflected that the chemical adsorption was the rating-limiting step in the adsorption process of LDH and BOC (Yu et al.,

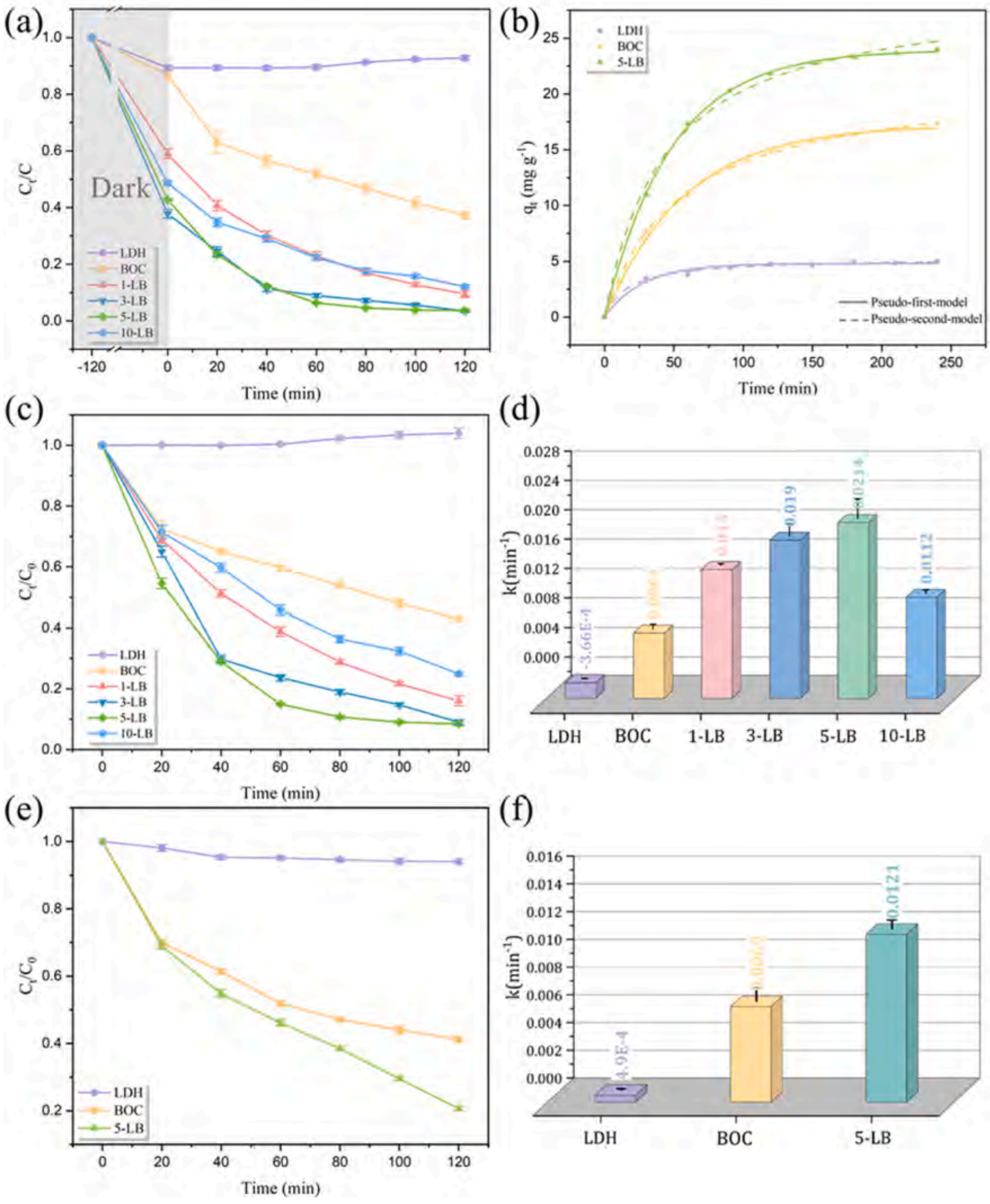

Fig. 3. (a) The total removal curves of CIP by different samples. (b) Equilibrium adsorption isotherms of CIP onto 5-LB fitted with pseudo-first-model and pseudo-second-model at 298 K. (c) Photocatalytic degradation of CIP with time under the irradiation of visible light and (d) pseudo-first order rate constants of $Bi_{12}O_{17}Cl_2$, CoAl-LDH and their hybrids. (e) Photocatalytic degradation of BPA with time under the irradiation of visible light and (f) pseudo-first order rate constants of $Bi_{12}O_{17}Cl_2$, CoAl-LDH and 5-LB.

2021). For 5-LB, the pseudo-first-order model ($R^2 = 0.99968$) was more suitable, meanwhile, pseudo-second-order model ($R^2 = 0.99162$) also exhibited high degree of fit. This result indicating that the adsorption process of 5-LB was more inclined to physisorption interaction, although chemisorption also played an important role (Tang et al., 2018). Afterwards, adsorption isotherm models analysis interpreted (Fig. S3) that the Langmuir isotherm model showed better correlation than Freundlich isotherm model for LDH, BOC and 5-LB, which indicated that the monolayer adsorption is the main adsorption process of above materials toward CIP (Perez-Marin et al., 2007).

Subsequently, the photocatalytic performance of the as-prepared photocatalysts could be investigated. Fig. 3c showed that there was no reduction in the concentration of CIP in the presence of a pure LDH after 120 min of visible light irradiation, and BOC exhibited relatively higher activity with the degradation efficiency of 57.12%. Whereas, all the x-LB hybrids displayed higher photocatalytic degradation activity. This indicated that the synergistic effect between LDH and BOC played a significant role in the photocatalytic process, although LDH exhibited a poor CIP degradation performance. Furthermore, the coupling content of LDH highly affected the degradation effect of CIP.

Specifically, the photocatalytic degradation efficiency increased gradually with the rise of LDH content from 1 wt% to 5 wt%, and 5-LB

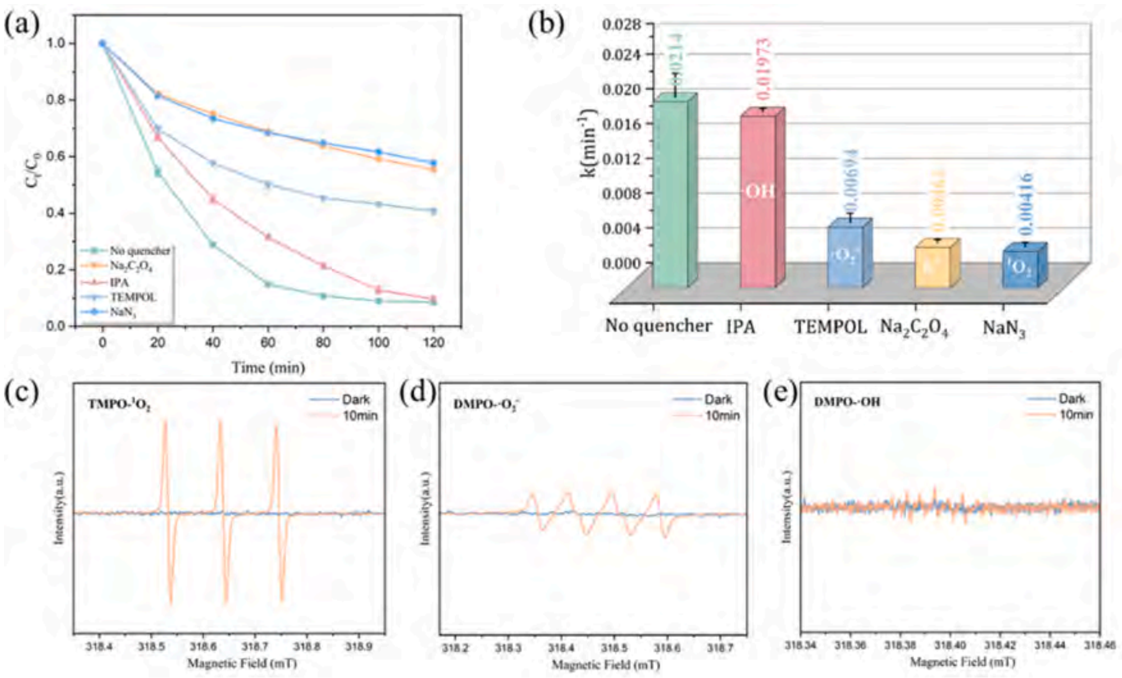

Fig. 4. (a) CIP degradation curves over 5-LB alone and with different quenchers under visible light irradiation and (b) the corresponding rate constants. ESR signals for (c) TMPO-$^1O_2$, (d) DMPO-•O_2^- and (e) DMPO-•OH over 5-LB sample.

exhibited the optimum performance, where 91.49% of CIP was decomposed. However, further increasing the coupling content of LDH to 10 wt% led to the attenuation of photocatalytic effect. This phenomenon might be due to that the increased Co^{2+} or Al^{3+} contacted with BOC, more exposed heterojunction sites for charge transfer were built up, but the quality and quantity of effective heterointerfaces favorable for charge transfer decreased which in turn reduced photocatalytic performance on the other hand (Wu et al., 2018). Thus, the control over the ratio of LDH to BOC was essential to achieve optimal photocatalytic performance. Meanwhile, the degradation kinetics curves have been fitted according to the pseudo-first-model and the values of rate constants (k) were shown in Fig. 3d. It was obvious that the CIP degradation rate was the fastest for 5-LB (0.0214 min^{-1}). Besides, the photocatalytic activity of 5-LB was further estimated toward the photodegradation of a typical endocrine disrupter (Bisphenol A, BPA). The photodegradation efficiency could reach 79.37% over 5-LB (Fig. 3e), giving a degradation rate of 0.0121 min^{-1} under visible light irradiation. The degradation rate of 5-LB was almost 1.75 and 24.69 folds higher than that of pure BOC and pure LDH (Fig. 3f). Furthermore, the stability of the 5-LB was investigated to ensure that this activity was reproducible over sequential treatment cycles. As exhibited in Fig. S4, after three repeated treatments, 5-LB still possessed an excellent removal capacity for CIP, and the CIP degradation efficiency was 84.84% on the third cycling run, slightly lower than that of the initial round (91.49%). In brief, these results reflected the potential advantages of 5-LB for ameliorating concerns with POPs in real systems.

3.3. *Optical and photoelectrochemical property*

In order to understand the reasons for the excellent photocatalytic performance, the optical-electrical properties of the photocatalysts have also been studied by UV-vis spectrum (UV-vis DRS) and photoelectrochemical tests. As illustrated in Fig. S5a, pure BOC exhibited a strong absorption from the ultraviolet to visible light range, and its band gap absorption edge was around 580 nm. Bare LDH displayed two distinct absorption bands, where the one that appeared in the UV range could be assigned to ligand-to-metal charge transfer ($O^{2-} \rightarrow M^{n+}$), and the other broad band centered around 500 nm was attributable to d–d transitions of octahedral Co^{2+} within the LDH layer (Kumar et al., 2017). This typical light absorption of LDH in the visible range could also be observed in the 5-LB composite, implying the strong interaction between BOC and LDH in the resulting heterojunction. Notably, compared with BOC, 5-LB exhibited a clear red shift in the absorption edge and an intensified light absorption in the visible region, which makes this hybrid a promising material for solar-light-driven catalytic applications. Additionally, the band gap of pure BOC and LDH were estimated to be 2.13 and 2.1 eV, respectively, according to the Tauc plot in Fig. S5b. Furthermore, the Mott-Schottky plots (Fig. S5c-d) exhibited that both BOC and LDH showed n-type semiconductor properties (Huang et al., 2017), and their V_{fb} were identified to be -0.9 and -0.81 V vs. SCE, respectively, corresponding to the conduction band (CB) potentials of -0.76 and -0.67 V vs. NHE, respectively. Hence, the valence band (VB) potentials were determined to be 1.37 and 1.43 V vs. NHE via the formula (E_g=E_{VB}-E_{CB}).

Fig. S5e clearly displayed that the photocurrent intensity of 5-LB was much higher than that of bare BOC and LDH, indicating the enhanced separation efficiency of photo-induced electron-hole pairs. Simultaneously, Fig. S5f depicted that the 5-LB possessed the lowest charge migration resistance, which confirmed that the formation of Co-Cl bond between BOC and LDH expedited the transfer of photo-excited charges. Therefore, it was reasonably induced that the boosted photochemical properties promoted the photocatalytic performance. Furthermore, the photoluminescence (PL) analysis (Fig. S6) showed that the emission peak of 5-LB hybrid was lower than that of pure LDH and pure BOC, which further confirmed that the recombination of photogenerated carriers were effectively suppressed, because of the interfacial charge transfer between LDH and BOC.

3.4. *Role of Reactive Species in CIP Degradation*

Chemical quenchers were applied to the experimental solutions to elucidate the contribution of specific reactive species to CIP degradation. Fig. 4a showed the extents of CIP degradation after 120 min of irradiation for the blank control and solutions containing IPA, TEMPOL,

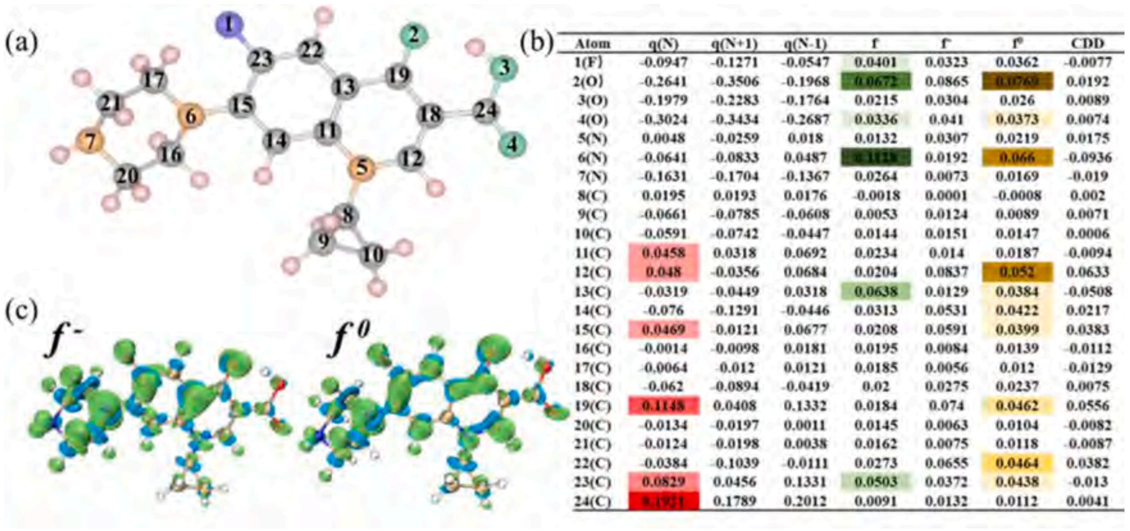

Atom	q(N)	q(N+1)	q(N-1)	f⁺	f⁻	f⁰	CDD
1(F)	-0.0947	-0.1271	-0.0547	0.0401	0.0323	0.0362	-0.0077
2(O)	-0.2641	-0.3506	-0.1968	0.0672	0.0865	0.0760	0.0192
3(O)	-0.1979	-0.2283	-0.1764	0.0215	0.0304	0.026	0.0089
4(O)	-0.3024	-0.3434	-0.2687	0.0336	0.041	0.0373	0.0074
5(N)	0.0048	-0.0259	0.018	0.0132	0.0307	0.0219	0.0175
6(N)	-0.0641	-0.0833	0.0487	0.1123	0.0192	0.066	-0.0936
7(N)	-0.1631	-0.1704	-0.1367	0.0264	0.0073	0.0169	-0.019
8(C)	0.0195	0.0193	0.0176	-0.0018	0.0001	-0.0008	0.002
9(C)	-0.0661	-0.0785	-0.0608	0.0053	0.0124	0.0089	0.0071
10(C)	-0.0591	-0.0742	-0.0447	0.0144	0.0151	0.0147	0.0006
11(C)	0.0458	0.0318	0.0692	0.0234	0.014	0.0187	-0.0094
12(C)	0.048	-0.0356	0.0684	0.0204	0.0837	0.052	0.0633
13(C)	-0.0319	-0.0449	0.0318	0.0638	0.0129	0.0384	-0.0508
14(C)	-0.076	-0.1291	-0.0446	0.0313	0.0531	0.0422	0.0217
15(C)	0.0469	-0.0121	0.0677	0.0208	0.0591	0.0399	0.0383
16(C)	-0.0014	-0.0098	0.0181	0.0195	0.0084	0.0139	-0.0112
17(C)	-0.0064	-0.012	0.0121	0.0185	0.0056	0.012	-0.0129
18(C)	-0.062	-0.0894	-0.0419	0.02	0.0275	0.0237	0.0075
19(C)	0.1148	0.0408	0.1332	0.0184	0.074	0.0462	0.0556
20(C)	-0.0134	-0.0197	0.0011	0.0145	0.0063	0.0104	-0.0082
21(C)	-0.0124	-0.0198	0.0038	0.0162	0.0075	0.0118	-0.0087
22(C)	-0.0384	-0.1039	-0.0111	0.0273	0.0655	0.0464	0.0382
23(C)	0.0829	0.0456	0.1331	0.0503	0.0372	0.0438	-0.013
24(C)	0.1921	0.1789	0.2012	0.0091	0.0132	0.0112	0.0041

Fig. 5. (a) Molecule structure of CIP. (b) NPA charge distribution and Fukui index of CIP. (c) The isosurface of Fukui index.

$Na_2C_2O_4$ and NaN_3 were approximately 91.49%, 90.37%, 59.22%, 44.50%, and 42.23%, respectively. Furthermore, the observed rate constants for CIP degradation were 0.0214, 0.01973, 0.00694, 0.00462, and 0.00416 min^{-1}, respectively (Fig. 4b). Using eqs 1-4, the relative contributions of •OH, $•O_2^-$, h^+, and $^1O_2$ to the overall CIP degradation were calculated to be 7.8%, 67.6%, 78.4%, and 72.8%, respectively. Note that the contributions sum to more than 100% because the generation of $^1O_2$ involved $•O_2^-$ and h^+ (eq. 8-10 and eq. 12). That is, when $•O_2^-$ or h^+ was quenched by a scavenger, the effect of $^1O_2$ was also inhibited (Wang et al., 2018, Zhang et al., 2016). Nevertheless, h^+ and $^1O_2$ production by the 5-LB photocatalytic system were found to be the major mechanism of CIP degradation. The ESR signals further verified the role of $^1O_2$ and $•O_2^-$ during the photocatalytic process (Fig. 4c-e). At the same irradiation point-in-time (10 min), the signal intensity of TMPO-$^1O_2$ was much stronger than DMPO-$•O_2^-$, and the signal intensity of DMPO-•OH was not obvious, indicating that the $^1O_2$ was the major reactive radical, followed by $•O_2^-$, and the •OH only played a minor role.

3.5. Degradation Pathways of CIP

To elucidate the photocatalytic mechanisms associated with CIP degradation, transformation products were identified by samples collected at 0, 60 and 120 min of irradiation for LC-MS analysis. The total MS spectra of possibly molecular intermediates at different reaction time were listed in Figs. S7 and S8, and 12 major transformation products were confirmed (Table S3). Apparently, the peak intensity of CIP molecule (m/z = 332) gradually decreased with the illumination time, while the peak intensity of the substances with smaller m/z values were first increase with irradiation time and then decrease upon further irradiation, which means that CIP was gradually degraded into small molecule products by 5-LB, and further illumination mineralized these products. Furthermore, the TOC removal experiment (Fig. S9) manifested that 5-LB can mineralize CIP more efficiently, and 66.3% of CIP was mineralized into inorganic small molecules (CO_2 and H_2O etc.) after 2h illumination.

To better examine the mechanisms that produced the 12 identified

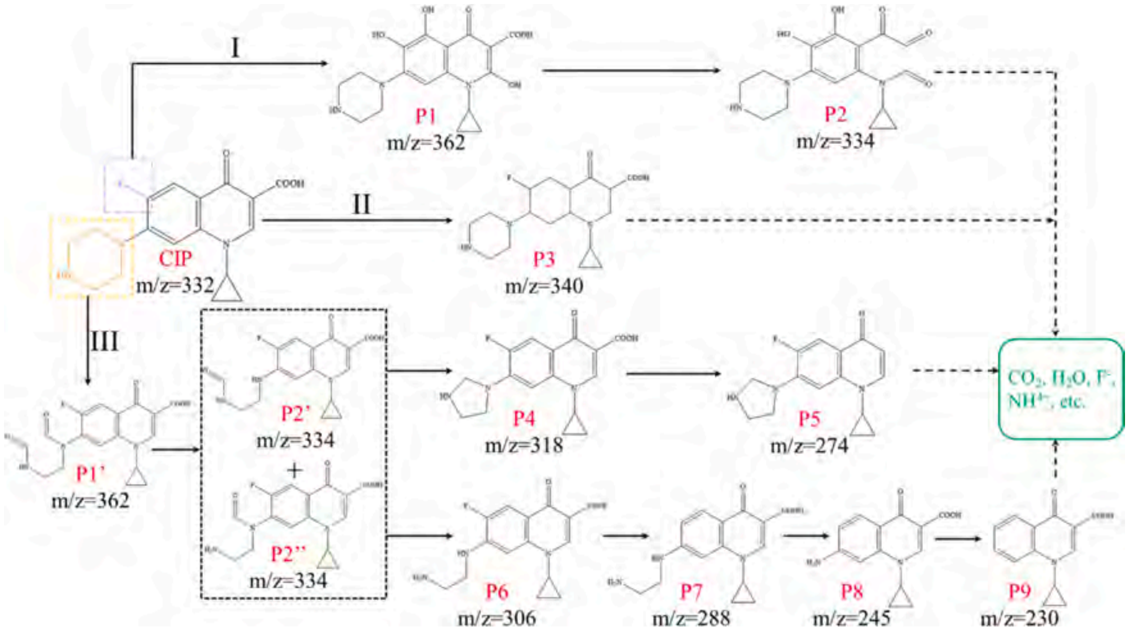

Fig. 6. The possible pathways for CIP degradation by 5-LB under the irradiation of visible light.

transformation products during photocatalysis of CIP, the NPA charge distribution and Fukui index were used to predict the sites of reactive species attack. The results of this analysis were summarized in Fig. 5. According to Fukui function theory, a high f^- value suggests that an atom is more like to be attacked by electrophilic reagent (h^+, $^1O_2$), a high positive point charge indicates the likelihood of $\bullet O_2^-$ attack (nucleophilic reaction), and a high f^0 value indicates that an atom is likely to be attacked by and •OH. The 6N, 2O, 13C, 23C, 1F and 4O positions exhibited high f^- values, suggesting the potential for h^+ and $^1O_2$ attack. The 24C, 19C, 23C, 12C, 15C and 11C positions displayed high positive point charges, and so these positions are expected to undergo preferential attack by $\bullet O_2^-$. High f^0 values were calculated for the 2O, 6N, 12C, 22C,19C and 23C positions, demonstrating that these sites may be directly attack by •OH (Li et al., 2021).These analyses were used with the identified transformation products to propose a tentative CIP photocatalytic pathway for the 5-LB−vis system (Fig. 6).

Pathway I was mainly a defluorination and hydroxylation process, which has been widely reported for degradation of fluoroquinolones (Lai et al., 2019, Wen et al., 2018). Specifically, the transformation from CIP to P1 was subjected to attacking at 1F (f^-=0.0401), 23C (q=0.0829, f^-=0.0503, f^0=0.0438), 22C (f^0=0.0464), and 12C (q=0.048, f^0=0.052) which leads to the cleavage of the C–F bond of CIP and the addition of a hydroxyl. Then the quinolone ring was broken, resulting in the formation of P2. In pathway II, it is detected that the intermediate product P3 was generated through the nucleophilic addition reaction, which is consistent with the nucleophilic site calculated by DFT. This mechanisms align with previous reports of photocatalysis of CIP antibiotics by TiO_2 (Hu et al., 2020).

Pathway III was the aldehyde reaction. According to the Fukui index, 6N position is most vulnerable to active species in piperazine rings, but it is difficult for 6N to accept radical addition due to saturation sites and steric hindrance. Meanwhile, due to the strong electron-withdrawing property of tertiary amine (6N), the α-carbon (17C) in piperazine ring became the next most susceptible position to be attacked by surrounding active species (Zheng et al., 2018). $^1O_2$ attacked the 17C in CIP to form endoperoxide (Eq. 5), which would further decompose to form acetaldehyde groups in a similar manner as that reported by Li et al.(Li et al., 2021, Liu et al., 2021, Wei et al., 2015). The formed product P1' were prone to be attacked by H^+ and subsequent hydrolysis to generated P2' and P2'' isomers (Chen et al., 2019). Furthermore, the aldehyde groups decomposed, resulting in formation of the P4 and P6. Ultimately, the identified products from all four pathways were photodegraded into smaller, oxygen-containing compounds and then being mineralized into water and carbon dioxide.

3.6. Photocatalytic mechanism governing the 5-LB photocatalytic system

On the basis of the above results and the energy levels of CoAl-LDH and $Bi_{12}O_{17}Cl_2$, the mechanism shown in Fig. 7 was proposed for 5-LB photocatalytic system. The BOC nanosheets were evenly immobilized on the surface of LDH in a plane-to-plane manner via Co-Cl bond. Compared with pure BOC nanosheets, the LDH nanosheets as substrate material suppressed the agglomeration of BOC, thereby the relatively higher surface-volume ratio made more adsorption sites of BOC be exposed. This allowed more POPs molecules to be adsorbed onto the BOC surface during the dark reaction stage, which was conducive to further degradation. Under visible-light illumination, both LDH and BOC could be activated into excited state and generated electrons and holes (see eq 6-7). Considering the stagger arrangement of band positions for BOC and LDH, the photoexcited electrons could thermodynamically transfer from the CB of BOC to the CB of LDH, whereas holes migrated oppositely in the VB due to the built-in electric field at the interface. Therefore, the photoexcited electrons and holes were effectively separated in micro-space.

$$\mathrm{LDH} + \mathrm{hv} \rightarrow \mathrm{LDH} + h^+ + e^- \tag{6}$$

$$\mathrm{BOC} + \mathrm{hv} \rightarrow \mathrm{BOC} + h^+ + e^- \tag{7}$$

Since the CB potential of LDH was more negative than the standard reduction potential of $O_2/\bullet O_2^-$ (- 0.33 eV), the conduction band e^- can be captured by dissolved oxygen to form $\bullet O_2^-$ (see eq 8). Subsequently, the $\bullet O_2^-$ reacts with H^+ (eq 9) to produce $^1O_2$ (eq 10) and •OH (eq 11) (Chen et al., 2019). Meanwhile, $\bullet O_2^-$ can also be oxidized by h^+ to form $^1O_2$ (eq 12) (Luo et al., 2021, Wang et al., 2019). In addition, the free radical trapping experiments show that the contribution of $\bullet O_2^-$ is lower than that of $^1O_2$, which means that the generation of $^1O_2$ also experienced other pathways, such as dissolved oxygen from water (eq. 13) (Liang et al., 2019, Zhao et al., 2019). The h^+ gathered on the VB of BOC with a potential of 1.37 eV is difficult to react with water or HO^- to form •OH. Thus, the •OH in the 5-LB photocatalytic system was derived from $\bullet O_2^-$-initiated reactions, and the ESR results showed that the generation of •OH was limited. This explained why •OH the played a negligible role in the degradation of CIP, while the h^+ and $^1O_2$ dominated the CIP transformation.

$$e^- + O_2 \rightarrow \bullet O_2^- \tag{8}$$

$$\bullet O_2^- + H^+ \rightarrow HO_2^\bullet \tag{9}$$

$$2HO_2^\bullet \rightarrow H_2O_2 + {}^1O_2 \tag{10}$$

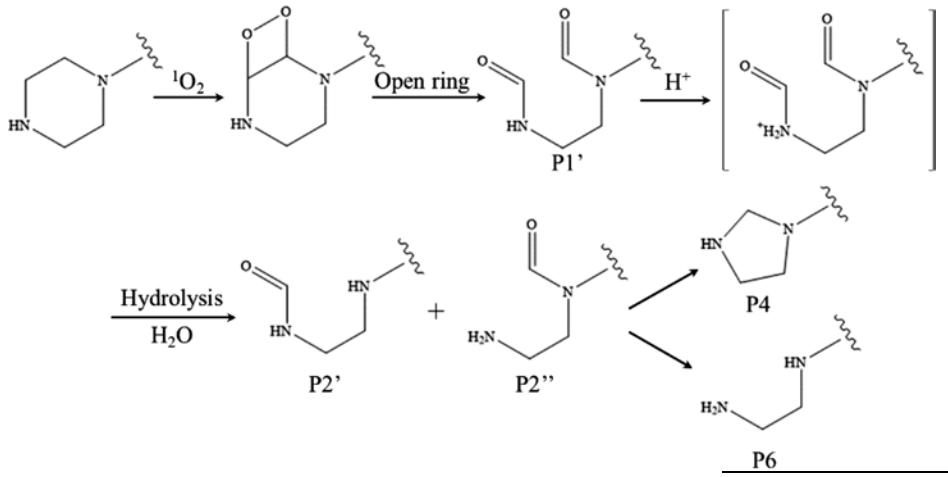

(5)

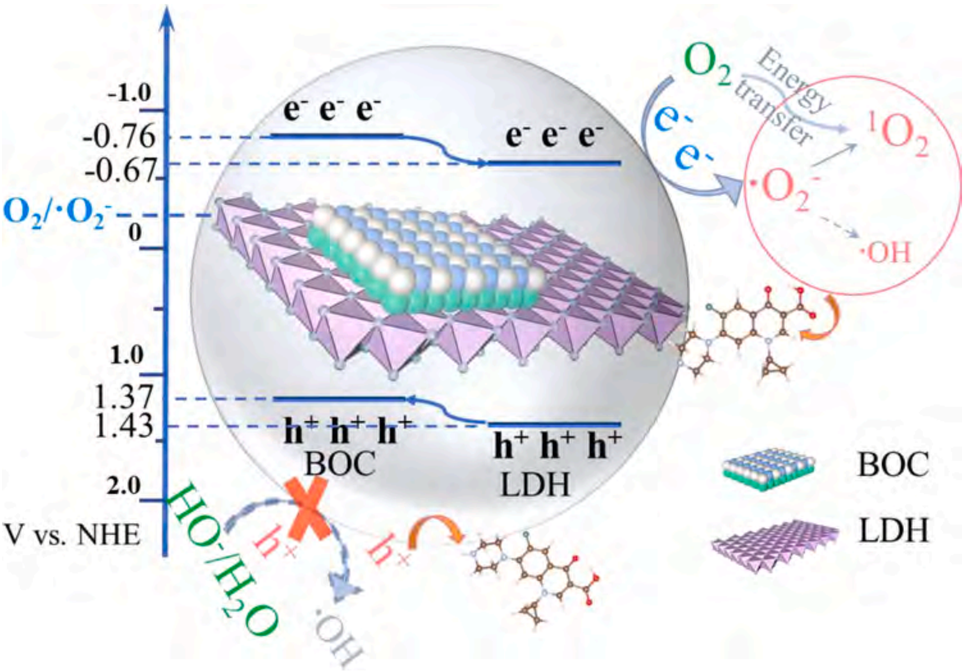

Fig. 7. The photocatalytic mechanism for 5-LB composites.

$$H_2O_2 + e^- \rightarrow \bullet OH + OH^- \quad (11)$$

$$\bullet O_2^- + h^+ \rightarrow {}^1O_2 \quad (12)$$

$$^3O_2 \rightarrow {}^1O_2 \text{ (energy transfer)} \quad (13)$$

3.7. Effects of water quality and interfering substances on CIP photocatalysis

The effect of pH value on the photocatalytic performance was shown in Fig. 8a and Fig. S10a. The observed rate constant for CIP degradation increased from 0.00357 min^{-1} at pH 3.0 to 0.0181 min^{-1} at pH 9.0, then decreased to 0.0101 at pH 11.0. This change trend was related to the surface properties of the photocatalyst and the states of the CIP molecules. As known, the CIP molecule can form five molecular species including CIP^{3+} species (pH<3.01), CIP^{2+} species (3.01<pH<6.14), CIP^{+} species (6.14<pH<8.70), $^{-}CIP^{+}$ species (8.70<pH<10.58) and CIP^{-} species (pH>10.58) (Yu et al., 2021). Obviously, the pH value of 10.58 is the watershed of the states of CIP molecules. Meanwhile, the different pH value leaded to the alterations in the Zeta potentials of 5-LB, and the results were shown in Fig. 8b. When the pH was in the range of 3-9, the surface of 5-LB possessed positive charges with a downward

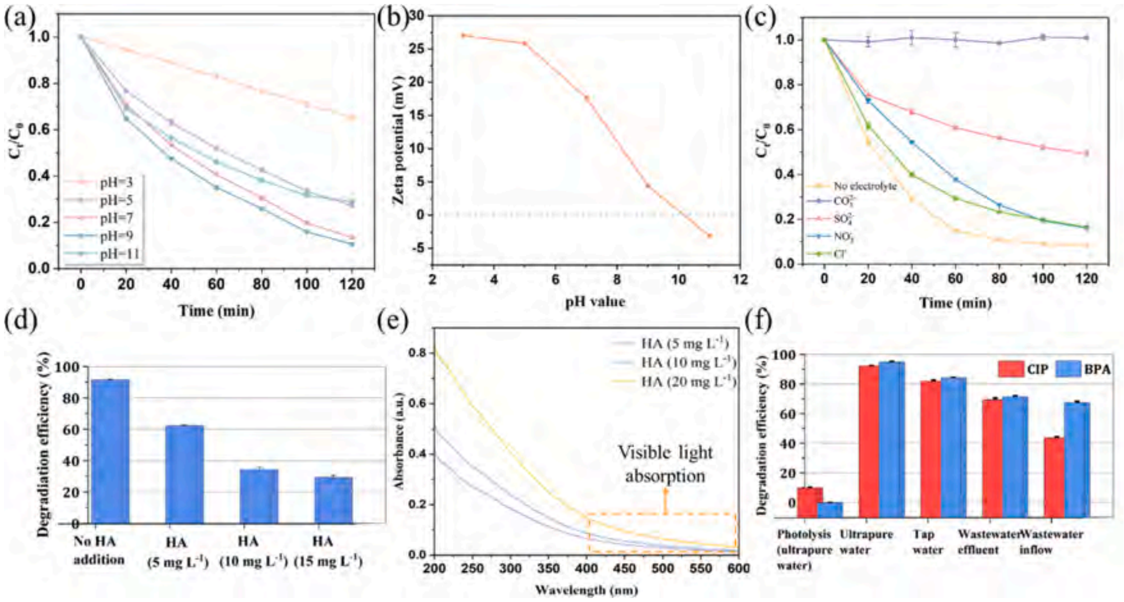

Fig. 8. The visible light driven photocatalytic performance of 5-LB for the degradation of CIP with the influence of (a) pH values, (c) anion species and (d) HA. (b) Zeta potential curves of 5-LB at different pH values. (e) UV−vis absorbance spectra of solutions containing different concentrations of HA. (f) Photocatalytic degradation efficiency of CIP and BPA in different water matrices by 5-LB under real sunlight irradiation.

trend, thus the electrostatic repulsion with CIP species was gradually diminished, which favored the attachment of CIP molecules to the photocatalytic active sites on the surface of 5-LB. Nevertheless, the surface of 5-LB was negatively charged at pH value of 11, where CIP molecules possessed the same electronegativity, indicating that the repulsive force between 5-LB and the deprotonated CIP was intensified and thereby led to an inferior CIP degradation efficiency. The results of adsorption experiments (Fig. S10b) almost agreed with the above conclusions.

The effects of water quality constituents on the performance for CIP photocatalysis were shown in Fig. 8c. Among the studied anions, the multivalent anions (SO_4^{2-}, CO_3^{2-}) indicated a more adverse effect than monovalent anions (Cl^- and NO_3^-) on photocatalytic CIP degradation. This is probably due to the stronger adsorption of multivalent ions than monovalent ions on electropositive photocatalyst surface, which consequently hindered the reaction of the CIP molecules with the active site. Thus, the amount of CIP molecules attached to the surface of 5-LB was decreased. The adsorption experiment well evidenced this phenomenon (Fig. S10c). It was obvious that the adsorption of CIP molecules on 5-LB was severely inhibited by CO_3^{2-}, while Cl^- and NO_3^- exerted little influence. Besides, the CO_3^{2-} can hydrolyze to generate OH^- ions and HCO_3^- ions, leading to the enhancement of the pH value (from 5.6 to 11.7), which is detrimental to photocatalytic activity (Fig. 8a). Furthermore, the different effects of the various ions can also attribute to the reaction kinetics between the active species and anions. For example, it is reported that CO_3^{2-} possess high ability of hole-capture, and the rate constant for CO_3^{2-} reaction with •OH to be 3.7×10^8 M^{-1} s^{-1} (David Behar 1970, Tan et al., 2019). Humic acid (HA), composed of aromatics and various functional groups, is complex organic molecules produced by the decomposition of plant and animals, and widely exists in natural water. Therefore, it is necessary to understand the effect of HA on 5-LB photocatalytic activity. As Fig. 8d exhibited, the degradation efficiency of CIP was significantly restrained by the HA, and the inhibitory effect increased with the concentration of HA. This may be due to the competitive interaction of HA with reactive species and light-screening effects induced by the conjugated double bonds chromophoric structure of HA in the visible region (Fig. 8) (Yang et al., 2021). Meanwhile, HA with negative charges is easily adsorbed to the surface of 5-LB and block the active sites, which impedes the adsorption of CIP to the surface of 5-LB (Fig. S10d), thereby inhibiting the photodegradation of CIP. Recently, the ubiquitous microplastics in aquatic environment has attracted wide attention (Feng et al., 2021). In this case, polystyrene (PS) particles were added into the reaction system to evaluate the effect of microplastics on 5-LB photocatalytic system (Fig. S10e). Interestingly, relatively lower concentrations of PS (10 mg L^{-1}) reduced the degradation rate of CIP but had little effect on the final degradation effect. However, higher concentration of 20 mg L^{-1} inhibited the degradation efficiency obviously, and only 80.18% of CIP was degraded. Similarly, the reduction of degradation efficiency could also be attributed to the contact restraint of CIP with 5-LB (Fig. S10f).

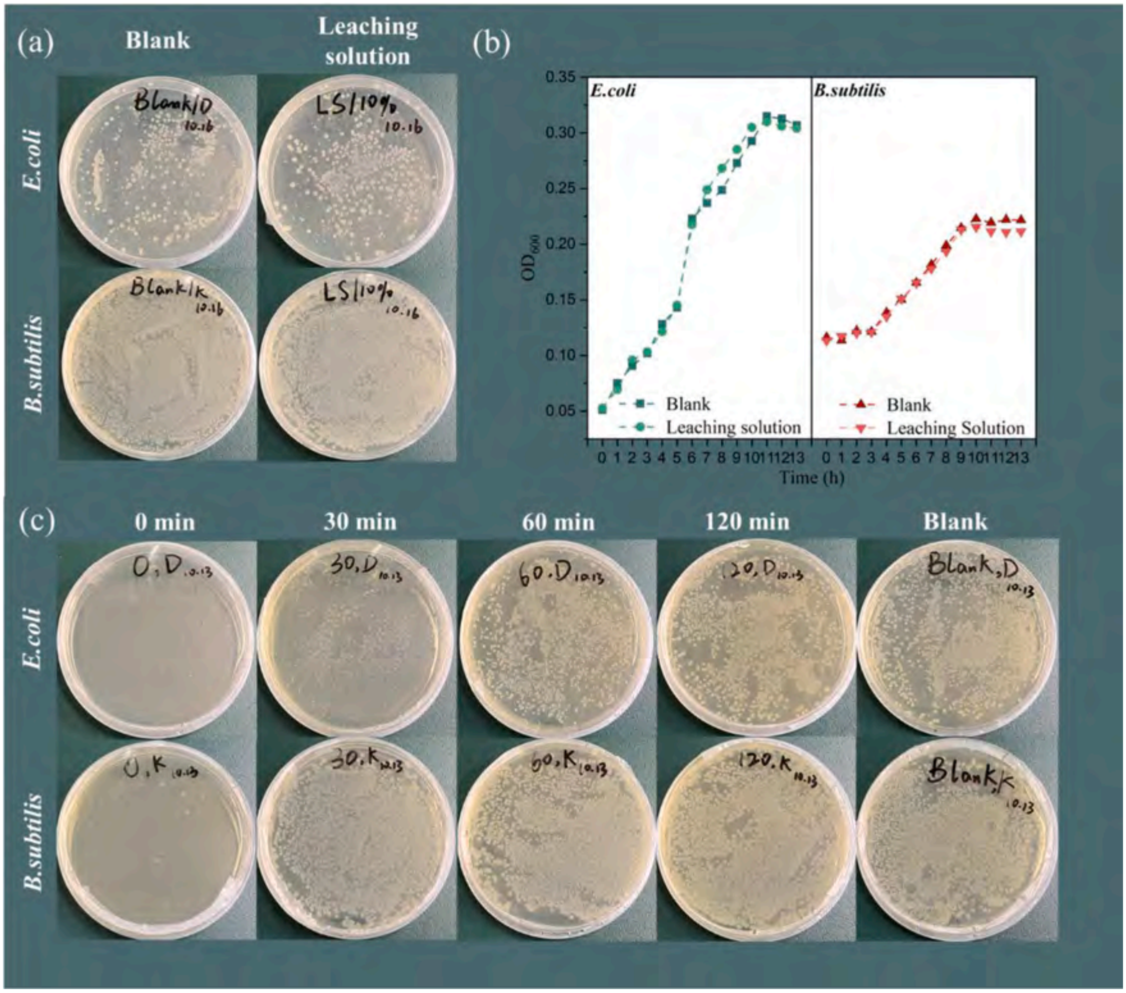

Fig. 9. (a) Photographs of bacterial colonies (*E.coli* and *B. subtilis*) formed on LB-agar plates with and without 5-LB leaching solution addition. (b) Growth curves of *E. coli* and *B.subtilis* in the addition of 5-LB leaching solution for 13 h. (c) Photographs of bacterial colonies (E.coli and B. subtilis) formed on LB-agar plates with the addition of CIP solutions treat in the 5-LB-vis system by different times (0 min, 60 min and 120 min), and blank represents no CIP solution added.

To better evaluate the suitability of the 5-LB to degrade POPs under environmental conditions, CIP and BPA degradation were studied in different water matrices under the natural sunlight illumination. The primary chemical properties of the real water matrices were shown in Table S4. As indicated in Fig. 8f, CIP had a weak photolysis under natural sunlight, while BPA hardly underwent photolysis under natural sunlight irradiation. Besides, the observed degradation efficiency for CIP in ultrapure water, tap water, wastewater effluent, and wastewater inflow were 92.47%, 82.17%, 69.67%, and 44.07%, respectively, and that of BPA were 95%, 84.37%, 71.63%, and 67.70%, respectively. Surprisingly, the photocatalytic performance of 5-LB in ultrapure water under natural sunlight illumination was even slightly better than that of xenon lamp. In view of the strong light intensity of xenon lamp, we believe that the superior photocatalytic effect under natural sunlight may be caused by the unfiltered ultraviolet light and the thermal effect. In order to verify this hypothesis, we used an AM 1.5G filter to provide simulated sunlight, and the results and related analysis were shown in Fig. S11. Ultrapure water exhibited the fastest CIP and BPA degradation due to the absence of reactive species scavenging or light screening. Compared to ultrapure water, the degradation of CIP and BPA was inhibited in environmental waters, especially in wastewater inflow, due to the scavenging effects caused by organic (TOC $= 6.48$ mg L^{-1}, COD$=$ 85.8 mg L^{-1}) and inorganic matters (Cl$^{-} = 23.1$ mg L^{-1}, SO$_4^{2-} = 21.2$ mg L^{-1}). These results suggested that 5-LB-sunlight photocatalytic system for ameliorating concerns with POPs are most applicable in after-stage of water treatment.

3.8. *Toxicity assessment using E.coli and B.subtilis as indicators*

The toxicity effects of the 5-LB photocatalysts and CIP as well as its photocatalytic degraded intermediates were assessed by their impacts on the surviving bacterial colonies density compared to that of the blank. As exhibited in Fig. 9a, the introduction of 5-LB leaching solution did not significantly change the bacterial colonies density, compared to the blank sample. Similarly, the growth curves of *E.coli* and *B.subtilis* (Fig. 9b) further demonstrated the negligible effects of 5-LB on bacteria, manifesting that 5-LB cannot cause secondary pollution to the ecological environment during a round of photocatalytic treatment.

Fig. 9c displayed that no *E.coli* colony and a few *B. subtilis* colonies were observed respectively, on the culture dishes with the addition of original CIP molecules (photocatalytic treatment for 0 min), indicating that the CIP molecules had strong inactivation effect on *E.coli* and *B. subtilis*. However, when the CIP molecules were photocatalyzed for a certain time, their toxicity effects on the two bacteria gradually weakened. Furthermore, compared with the blank group, the toxicity effect of CIP molecules with 120 min of photocatalytic treatment on the growth of *E.coli* and *B.subtilis* was negligible, signifying that 5-LB can significantly degrade CIP molecules into less toxic intermediates or even completely mineralize CIP molecules after 120 min of light exposure. This experimental phenomenon was consistent with the toxicity evaluation results of degradation intermediates by Toxicity Estimation Software (T.E.S.T, Fig. S12).

4. Conclusion

The photocatalytic degradation of POPs using eco-friendly 5-LB photocatalyst was evaluated in water/wastewater under both simulated visible light and actual solar light irradiation, and the toxicity of the photocatalyst and treated solution was assessed.

- 5-LB photocatalysts exhibited excellent photocatalytic performance, which could degrade 91.49 % (92.47 %) of CIP and 79.37 % (95 %) of BPA with 2h of visible light (actual solar light) irradiation. This can be attributed to the successful formation of Co-Cl bonded heterojunction between 2D $Bi_{12}O_{17}Cl_2$ and 2D CoAl-LDH, which induces broad absorption spectrum, rapid photogenerated carrier migration and abundant active site exposure. Furthermore, 5-LB shows good reusability over three cycles for photocatalytic CIP degradation under visible light irradiation.
- The degradation process dominated by h^{+} and $^{1}O_2$. The active atoms of CIP molecule with high Fukui index interpret the C-F bond cleavage, ring hydroxylation, nucleophilic addition and aldehyde reaction under the attack of reactive radicals.
- The pH value, organic matter (e.g. HA) and suspended matter (e.g. PS) are found to significantly influence the photocatalytic performance. Multivalent anions (CO_3^{2-}, SO_4^{2-}) have more adverse effects than monovalent anions (Cl^{-}, NO^{3-}) on the photocatalytic degradation. Therefore, under illumination of actual sunlight, 5-LB perform well in tap water and wastewater effluent, while unsatisfactory in wastewater inflow. Thus, 5-LB photocatalytic technology is more suitable to apply in the after-stage of water treatment.
- In the toxicity assessment, 5-LB photocatalyst itself and the treated CIP solution exhibited negligible effects on the growth of *E.coli* and *B. subtilis*. It reflects the potential of photocatalytic degradation using 5-LB for the green and safe application in real water treatment.

Declaration of Competing interest

The authors declare that they have no known competing financial interests or personal relationships that could have appeared to influence the work reported in this paper.

Acknowledgements

This work was supported by the National Natural Science Foundation of China (72088101, 51979101, 51739004, 51521006), the Hunan Science & Technology Innovation Program (2018RS3037), the Natural Science Foundation of Hunan Province (2019JJ20002).

Supplementary materials

Supplementary material associated with this article can be found, in the online version, at doi:10.1016/j.watres.2022.118558.

References

Chen, P., Blaney, L., Cagnetta, G., Huang, J., Wang, B., Wang, Y., Deng, S., Yu, G., 2019. Degradation of Ofloxacin by Perylene Diimide Supramolecular Nanofiber Sunlight-Driven Photocatalysis. Environ. Sci. Technol. 53 (3), 1564–1575.

David Behar, G.C., Duchovny, Itzhak, 1970. Carbonate Radical in Flash Photolysis and Pulse Radiolysis of Aqueous Carbonate Solutions. J. Phys. Chem. 74, 2206–2210.

Dong, H., Zeng, G., Tang, L., Fan, C., Zhang, C., He, X., He, Y., 2015a. An overview on limitations of TiO_2-based particles for photocatalytic degradation of organic pollutants and the corresponding countermeasures. Water Res 79, 128–146.

Dong, Q., Fang, Y., Shao, Y., Mulligan, P., Qiu, J., Cao, L., Huang, J., 2015b. Solar cells. Electron-hole diffusion lengths >175 mum in solution-grown $CH_3NH_3PbI_3$ single crystals. Science 347 (6225), 967–970.

Dou, Y., Zhang, S., Pan, T., Xu, S., Zhou, A., Pu, M., Yan, H., Han, J., Wei, M., Evans, D. G., Duan, X., 2015. TiO_2@Layered Double Hydroxide Core-Shell Nanospheres with Largely Enhanced Photocatalytic Activity Toward O_2 Generation. Adv. Funct. Mater. 25 (15), 2243–2249.

Feng, S., Lu, H., Yao, T., Xue, Y., Yin, C., Tang, M., 2021. Spatial characteristics of microplastics in the high-altitude area on the Tibetan Plateau. J. Hazard. Mater. 417, 126034.

Ganguly, P., Harb, M., Cao, Z., Cavallo, L., Breen, A., Dervin, S., Dionysiou, D.D., Pillai, S. C., 2019. 2D Nanomaterials for Photocatalytic Hydrogen Production. ACS Energy Lett 4 (7), 1687–1709.

Guo, J., Jiang, L., Liang, J., Xu, W., Yu, H., Zhang, J., Ye, S., Xing, W., Yuan, X., 2021. Photocatalytic degradation of tetracycline antibiotics using delafossite silver ferrite-based Z-scheme photocatalyst: Pathways and mechanism insight. Chemosphere 270, 128651.

Hu, X., Hu, X., Peng, Q., Zhou, L., Tan, X., Jiang, L., Tang, C., Wang, H., Liu, S., Wang, Y., Ning, Z., 2020. Mechanisms underlying the photocatalytic degradation pathway of ciprofloxacin with heterogeneous TiO_2. Chem. Eng. J. 380, 122366.

Huang, H., Dai, B., Wang, W., Lu, C., Kou, J., Ni, Y., Wang, L., Xu, Z., 2017. Oriented Built-in Electric Field Introduced by Surface Gradient Diffusion Doping for Enhanced Photocatalytic H_2 Evolution in CdS Nanorods. Nano. Lett. 17 (6), 3803–3808.

Kumar, S., Isaacs, M.A., Trofimovaite, R., Durndell, L., Parlett, C.M.A., Douthwaite, R.E., Coulson, B., Cockett, M.C.R., Wilson, K., Lee, A.F., 2017. P25@CoAl layered double hydroxide heterojunction nanocomposites for CO_2 photocatalytic reduction. Appl. Catal., B 209, 394–404.

Lai, C., Zhang, M., Li, B., Huang, D., Zeng, G., Qin, L., Liu, X., Yi, H., Cheng, M., Li, L., Chen, Z., Chen, L., 2019. Fabrication of CuS/$BiVO_4$ (0 4 0) binary heterojunction photocatalysts with enhanced photocatalytic activity for Ciprofloxacin degradation and mechanism insight. Chem. Eng. J. 358, 891–902.

Li, J., Zhan, G., Yu, Y., Zhang, L., 2016. Superior visible light hydrogen evolution of Janus bilayer junctions via atomic-level charge flow steering. Nat. Commun. 7, 11480.

Li, N., Li, R., Duan, X., Yan, B., Liu, W., Cheng, Z., Chen, G., Hou, L., Wang, S., 2021. Correlation of Active Sites to Generated Reactive Species and Degradation Routes of Organics in Peroxymonosulfate Activation by Co-Loaded Carbon. Environ. Sci. Technol. 55 (23), 16163–16174.

Liang, C., Guo, H., Zhang, L., Ruan, M., Niu, C.-G., Feng, H.-P., Wen, X.-J., Tang, N., Liu, H.-Y., Zeng, G.-M., 2019. Boosting molecular oxygen activation ability in self-assembled plasmonic p-n semiconductor photocatalytic heterojunction of WO_3/Ag@Ag_2O. Chem. Eng. J. 372, 12–25.

Liu, H., Gao, Y., Wang, J., Ma, D., Wang, Y., Gao, B., Yue, Q., Xu, X., 2021. The application of UV/O_3 process on ciprofloxacin wastewater containing high salinity: Performance and its degradation mechanism. Chemosphere 276, 130220.

Liu, W., Li, Y., Liu, F., Jiang, W., Zhang, D., Liang, J., 2019. Visible-light-driven photocatalytic degradation of diclofenac by carbon quantum dots modified porous g-C_3N_4: Mechanisms, degradation pathway and DFT calculation. Water. Res. 151, 8–19.

Lu, Tian, Chen, Feiwu, 2011. Multiwfn: A multifunctional wavefunction analyzer. J Comput Chem.

Luo, J., Liu, Y., Fan, C., Tang, L., Yang, S., Liu, M., Wang, M., Feng, C., Ouyang, X., Wang, L., Xu, L., Wang, J., Yan, M., 2021. Direct Attack and Indirect Transfer Mechanisms Dominated by Reactive Oxygen Species for Photocatalytic H_2O_2 Production on g-C_3N_4 Possessing Nitrogen Vacancies. ACS Catal. 11, 11440–11450. https://doi.org/10.1021/acscatal.1c03103.

Perez-Marin, A.B., Zapata, V.M., Ortuno, J.F., Aguilar, M., Saez, J., Llorens, M., 2007. Removal of cadmium from aqueous solutions by adsorption onto orange waste. J. Hazard. Mater. 139 (1), 122–131.

Pi, Y., Li, X., Xia, Q., Wu, J., Li, Y., Xiao, J., Li, Z., 2018. Adsorptive and photocatalytic removal of Persistent Organic Pollutants (POPs) in water by metal-organic frameworks (MOFs). Chem. Eng. J. 337, 351–371.

Shang, J., Hao, W., Lv, X., Wang, T., Wang, X., Du, Y., Dou, S., Xie, T., Wang, D., Wang, J., 2014. Bismuth Oxybromide with Reasonable Photocatalytic Reduction Activity under Visible Light. ACS Catal 4 (3), 954–961.

Sun, H.B., Qin, P.F., Wu, Z.B., Liao, C.J., Guo, J.Y., Luo, S., Chai, Y.Z., 2020. Visible light-driven photocatalytic degradation of organic pollutants by a novel Ag_3VO_4/Ag_2CO_3 p-n heterojunction photocatalyst: Mechanistic insight and degradation pathways. J. Alloys Compd. 834, 155211.

Tan, T., Xie, J., Wang, W., Ping, H., Ma, P., Xie, H., Wang, W., Fu, Z., 2019. A bio-inspired strategy for enhanced hydrogen evolution: carbonate ions as hole vehicles to promote carrier separation. Nanoscale 11 (24), 11451–11456.

Tang, N., Niu, C.G., Li, X.T., Liang, C., Guo, H., Lin, L.S., Zheng, C.W., Zeng, G.M., 2018. Efficient removal of Cd(2+) and Pb(2+) from aqueous solution with amino- and thiol-functionalized activated carbon: Isotherm and kinetics modeling. Sci. Total. Environ. 635, 1331–1344.

Tang, Y., Wang, R., Yang, Y., Yan, D., Xiang, X., 2016. Highly Enhanced Photoelectrochemical Water Oxidation Efficiency Based on Triadic Quantum Dot/Layered Double Hydroxide/$BiVO_4$ Photoanodes. ACS Appl. Mater. Interfaces 8 (30), 19446–19455.

Wang, F., Feng, Y., Chen, P., Wang, Y., Su, Y., Zhang, Q., Zeng, Y., Xie, Z., Liu, H., Liu, Y., Lv, W., Liu, G., 2018. Photocatalytic degradation of fluoroquinolone antibiotics using ordered mesoporous g-C_3N_4 under simulated sunlight irradiation: Kinetics, mechanism, and antibacterial activity elimination. Appl. Catal., B 227, 114–122.

Wang, K., Li, Y., Zhang, G., Li, J., Wu, X., 2019. 0D Bi nanodots/2D Bi_3NbO_7 nanosheets heterojunctions for efficient visible light photocatalytic degradation of antibiotics: Enhanced molecular oxygen activation and mechanism insight. Appl. Catal., B 240, 39–49.

Wang, Y., Dou, L., Zhang, H., 2017. Nanosheet Array-Like Palladium-Catalysts Pdx/rGO@CoAl-LDH via Lattice Atomic-Confined in Situ Reduction for Highly Efficient Heck Coupling Reaction. ACS Appl. Mater. Interfaces 9 (44), 38784–38795.

Wang, Z., Wang, H., Zeng, Z., Zeng, G., Xu, P., Xiao, R., Huang, D., Chen, X., He, L., Zhou, C., Yang, Y., Wang, Z., Wang, W., Xiong, W., 2020. Metal-organic frameworks derived $Bi_2O_2CO_3$/porous carbon nitride: A nanosized Z-scheme systems with enhanced photocatalytic activity. Appl. Catal., B 267, 118700.

Wei, X., Chen, J., Xie, Q., Zhang, S., Li, Y., Zhang, Y., Xie, H., 2015. Photochemical behavior of antibiotics impacted by complexation effects of concomitant metals: a case for ciprofloxacin and Cu(II). Environ. Sci. Process Impacts 17 (7), 1220–1227.

Wen, X.-J., Niu, C.-G., Zhang, L., Liang, C., Guo, H., Zeng, G.-M., 2018. Photocatalytic degradation of ciprofloxacin by a novel Z-scheme CeO_2–Ag/AgBr photocatalyst: Influencing factors, possible degradation pathways, and mechanism insight. J. Catal. 358, 141–154.

Wu, Y., Wang, H., Sun, Y., Xiao, T., Tu, W., Yuan, X., Zeng, G., Li, S., Chew, J.W., 2018. Photogenerated charge transfer via interfacial internal electric field for significantly improved photocatalysis in direct Z-scheme oxygen-doped carbon nitrogen/CoAl-layered double hydroxide heterojunction. Appl. Catal., B 227, 530–540.

Xiong, J., Di, J., Xia, J., Zhu, W., Li, H., 2018. Surface Defect Engineering in 2D Nanomaterials for Photocatalysis. Adv. Funct. Mater. 28 (39).

Yang, J., Wang, H., Jiang, L., Yu, H., Zhao, Y., Chen, H., Yuan, X., Liang, J., Li, H., Wu, Z., 2022. Defective polymeric carbon nitride: Fabrications, photocatalytic applications and perspectives. Chem. Eng. J. 427, 130991.

Yang, X., Sun, H., Li, G., An, T., Choi, W., 2021. Fouling of TiO_2 induced by natural organic matters during photocatalytic water treatment: Mechanisms and regeneration strategy. Appl. Catal. B 294.

Yu, H., Huang, J., Jiang, L., Yuan, X., Yi, K., Zhang, W., Zhang, J., Chen, H., 2021. Steering photo-excitons towards active sites: Intensified substrates affinity and spatial charge separation for photocatalytic molecular oxygen activation and pollutant removal. Chem. Eng. J. 408, 127334.

Zhang, Z., Wang, J., Liu, D., Luo, W., Zhang, M., Jiang, W., Zhu, Y., 2016. Highly Efficient Organic Photocatalyst with Full Visible Light Spectrum through pi-pi Stacking of TCNQ-PTCDI. ACS Appl. Mater. Interfaces 8 (44), 30225–30231.

Zhao, S., Dai, Z., Guo, W., Chen, F., Liu, Y., Chen, R., 2019. Highly selective oxidation of glycerol over Bi/$Bi_{3.64}Mo_{0.36}O_{6.55}$ heterostructure: Dual reaction pathways induced by photogenerated $^1O_2$ and holes. Appl. Catal. B 244, 206–214.

Zheng, X., Xu, S., Wang, Y., Sun, X., Gao, Y., Gao, B., 2018. Enhanced degradation of ciprofloxacin by graphitized mesoporous carbon (GMC)-TiO2 nanocomposite: Strong synergy of adsorption-photocatalysis and antibiotics degradation mechanism. J. Colloid Interface Sci. 527, 202–213.

Zhu, L., Wu, Y., Wu, S., Dong, F., Xia, J., Jiang, B., 2021. Tuning the Active Sites of Atomically Thin Defective $Bi_{12}O_{17}Cl_2$ via Incorporation of Subnanometer Clusters. ACS Appl. Mater. Interfaces 13 (7), 9216–9223.